RSC Advances

PAPER

View Article Online
View Journal | View Issue

Cite this: *RSC Adv.*, 2016, **6**, 33022

Effect of Mn_3O_4 nanoparticle composition and distribution on graphene as a potential hybrid anode material for lithium-ion batteries†

Ismail Alperen Ayhan,[a] Qi Li,[a] Praveen Meduri,[b] Hyukkeun Oh,[a] Ganesh R. Bhimanapati,[a] Guang Yang,[a] Joshua A. Robinson[a] and Qing Wang*[a]

Received 21st December 2015
Accepted 28th March 2016

DOI: 10.1039/c5ra27343a

www.rsc.org/advances

Nanosized manganese oxide (Mn_3O_4) particles grown on reduced graphene oxide (rGO) have been prepared *via* a facile synthetic method with different weight ratios, as hybrid anode materials for high performance lithium ion batteries (LIBs). The Mn_3O_4/rGO hybrid materials have been characterized by a library of techniques to better understand the effect of the structure and composition of the hybrids on the electrochemical performance of LIBs. The results show that the Mn_3O_4 nanoparticles are homogenously dispersed on rGO nanosheets. By virtue of efficient electron conduction pathways and high surface area properties promoted by rGOs, the Mn_3O_4/rGO hybrid material used as an anode material exhibits an enhanced reversible capacity, cycling stability, and rate capability.

Introduction

Energy storage has become a major challenge in the twenty-first century.[1] To meet the needs of modern society and emerging ecological concerns, new alternative technologies have been developed to harvest and store sustainable clean energy over the past few decades. One of the best ways to generate electricity is through electrochemical conversion (chemical energy conversion to electrical energy), by sharing a common carrier, that is the electron. Compared to other energy storage systems, rechargeable lithium ion batteries (LIBs) are one of the greatest successes since they are a serious contender to better manage the renewable resources on earth, and to favor the deployment of electric vehicles so as to reduce pollution.[2]

Graphite is used as an anode in rechargeable batteries[3] due to its layered structure, low potential and excellent interfacial stability.[4] However, it has limited intercalation capacity (372 mA h g^{-1}) as LiC_6.[5] Thus, exploration of new carbonaceous hybrid materials can play a critical role to improve the anode performance of LIBs. As such, graphene-based hybrid materials have been widely investigated as anode materials for high-performance LIBs. Graphene can be used for housing active materials as a substrate because it can provide large surface area, efficient pathways for electron conduction, and chemical stability.[6–9] Among a variety of high capacity anode materials, metal oxides have been thoroughly studied due to their high theoretical capacities promoted *via* conversion reaction.[10] Mn_3O_4 is one of the most promising, abundant and non-toxic anode material[11] with high theoretical specific capacity (937 mA h g^{-1}). However, it shows capacity fading and poor cyclability due to intrinsically low electrical conductivity and high volume change.[11–13]

Recent studies indicate that Mn_3O_4 hybrid materials with derivatives of graphene facilitated charge transfer which enhances cycling behavior. It is found that a specific capacity of 900 mA h g^{-1} (based on the mass of Mn_3O_4) at 40 mA g^{-1} was retained after 5 cycles for the hybrid material of Mn_3O_4 nanoparticles on rGO formed by two-step solution-phase reactions.[14] Wang *et al.*[15] reported that Mn_3O_4/graphene prepared through ultrasonic-assisted synthetic route in ETA-water delivered 900 mA h g^{-1} (based on the mass of Mn_3O_4) at 40 mA g^{-1} for 20 cycles. Nam *et al.*[16] reported that Mn_3O_4/graphene composite fabricated by one-step *in situ* transformation method exhibited a reversible capacity of over 500 mA h g^{-1} (based on the mass of Mn_3O_4) at 60 mA g^{-1} for 40 cycles. However, the electrochemical performance of these hybrid materials is degraded after few tens of cycles by the aggregation of nanoparticles on the nanosheet surfaces due to the large volume expansion during charge/discharge cycles. Dimitrijevic *et al.*[17] lately reported that the volume fractions, particle size and inter-particle distance significantly affect the mechanical stability of graphene-based anode materials. They

[a]*Department of Materials Science and Engineering, The Pennsylvania State University, University Park, PA 16802, USA. E-mail: wang@matse.psu.edu*

[b]*Department of Chemical Engineering, Indian Institute of Technology Hyderabad, Kandi, Sangareddy, Telangana – 502285, India*

† Electronic supplementary information (ESI) available: TGA curves of MRG1, MRG2, MRG3 and rGO; table showing inter-particle distance analysis of the samples MRG1, MRG2 and MRG3; XRD patterns of the samples graphite, GO, and rGO; SEM images of the samples (a) bare Mn_3O_4, (b) MRG1, (c) MRG2 and (d) MRG3 hybrid materials; the particles of MRG2 sample determined using ImageJ software and the particle size distribution histogram; HAADF-STEM image of MRG2 sample and corresponding EDX elemental mapping images. See DOI: 10.1039/c5ra27343a

showed theoretically that the least inter-particle spacing has to be 1.5 times the particles' diameter. Liu *et al.*[18] also demonstrated experimentally that the yolk–shell design provides void spaces between particles which allows for the expansion and acts as a buffering zone.

In this study, we report on the improvement of the electrochemical performance by developing a hybrid anode material with optimizing inter-particle distance between Mn_3O_4 nanoparticles on rGOs. The Mn_3O_4/rGO hybrid materials are obtained *via* a facile *in situ* fabrication method, in which the particle size, inter-particle spacing and dispersion are examined and their influence on electrochemical performance is evaluated. It is found that the reversible capacity, good cycling stability, and rate capability are improved *via* optimizing the nanoparticle content in the hybrid material.

Experimental section

Synthesis of graphene oxide (GO)

GO was synthesized by a modified Hummers' method.[19] Graphite powder (2.5 g) and $NaNO_3$ (1.5 g) were mixed with concentrated H_2SO_4 (98 wt%, 80 mL) in an ice-bath. While stirring the mixture vigorously, 15 g of $KMnO_4$ was slowly added and the temperature was maintained below 20 °C. Then, the temperature was increased to 35 ± 3 °C, and the stirring was continued for another 3 h. Thereafter, the mixture was diluted with 150 mL deionized (DI) water and 10 mL hydrogen peroxide solution (30 wt%) was slowly added. The mixture was then filtered through metrical membrane filters (pore size 0.45 μm) and washed with 1 : 10 HCl solution several times to remove metal ions, and then washed with DI water to remove the acid. Subsequently, the final solid was dispersed again in DI water under sonication (200 W, 40 kHz, 5 h), which was followed by centrifugation at 4000 rpm for 30 min to further remove aggregations. Finally, the suspension was loaded into a petri dish and dried at 40 °C for 12 h in vacuum oven to obtain solid graphene oxide nanosheets.

Synthesis of Mn_3O_4/rGO hybrid

Mn_3O_4/rGO hybrid materials were fabricated using a facile *in situ* synthesis process. In a typical synthesis, GO (0.1 g) was dispersed in isopropanol (50 mL) by sonication for 3 h in a beaker to obtain highly homogenous dispersion. $MnCl_2 \cdot 4H_2O$ was added to GO dispersion and dissolved with the aid of vigorous magnetic stirring for 1 h. Next, the solution was heated to approximately 85 °C with refluxing while stirring. When the solution reached 85 °C, $KMnO_4$ (0.12 M) (2 : 3 molar ratio with $MnCl_2 \cdot 4H_2O$) dissolved in DI water was added rapidly and the mixture was kept stirring for 30 min at 85 °C. After refluxing, the mixture was cooled to room temperature and precipitated by centrifuge. The resulting precipitate was washed several times with DI water and re-dispersed in DI water (100 mL) with ultrasonic bath for 30 min. NaOH solution (1 M) was slowly added under constant stirring for 10 min to keep the pH value at 10 or above. Hydrazine hydrate (0.03 mL) was injected into the above solution at 80 °C for GO reduction. After refluxing for 2 h followed by cooling to room temperature, the solution was filtrated and washed several times with DI water until filtrate became neutral. The resulting Mn_3O_4/rGO hybrid material was dried at 80 °C overnight. The weight of GO was kept constant in the hybrid materials and the weight loading ratios of $MnCl_2 \cdot 4H_2O$ to rGO was varied as 1 : 1, 2 : 1 and 3 : 1 that has been named as **MRG1**, **MRG2**, and **MRG3**, respectively. Separately, bare Mn_3O_4 nanoparticles and rGO nanosheets were fabricated through the same process.

Characterization of Mn_3O_4/rGO hybrid

The prepared materials were characterized by powder X-ray diffraction (XRD) using a PANalytical Empyrean X-ray Diffractometer performed at a voltage of 40 V and a current of 40 mA with Cu Kα radiation ($\lambda = 1.54$ Å) in the 2θ range from 5° to 70° at scan rate of 2° min^{-1}. The Raman Spectra were recorded using a WITec Confocal Raman Microscope with 488 nm wavelength incident laser light and a 100× objective. Morphologies were characterized by LEO 1530 MERLIN field emission scanning electron microscopy (FE-SEM, 20 kV). Particle size and dispersion of hybrid materials were investigated by transmission electron microscopy (TEM) (JEOL JEM-2010F, 200 kV). The particle size distribution was obtained using ImageJ software. High angle dark field (HAADF) and elemental mapping analysis were also carried out using scanning transmission electron microscopy (STEM) with a Super-X energy dispersive X-ray (EDX) detector configuration (FEI TALOS F200X, 200 kV). Thermal gravimetric analysis (TGA) was conducted on a TGA 2050 analyzer from 25 °C to 800 °C in airflow at a heating rate of 10 °C min^{-1}. The surface areas of Mn_3O_4/rGO hybrid materials were obtained by N_2 adsorption isotherm measured with a Micrometrics ASAP-2020 instrument.

Electrochemical analysis

The Mn_3O_4/rGO electrode materials were ground to a fine powder. The powder (~200 mg) as the active material was mixed with Super P carbon black (conductive additive) and PVDF (binder) with a weight ratio of 80 : 10 : 10. All three components were stirred in *N*-methyl-2-pyrrolidone (NMP) overnight to yield a uniform and viscous electrode slurry. The slurry was uniformly coated with doctor blade onto a copper foil. After coating, the film was dried at room temperature overnight and punched into circular electrodes which are then dried in a vacuum oven for 12 h at 80 °C. The loading densities of the electrodes are ~1 mg cm^{-2}. The coin cells were assembled in an argon-filled glovebox with lithium foil as the counter electrode, Celgard membrane as the separator, and a solution of 1.0 M $LiPF_6$ (dissolved in EC : PC : DMC with a 1 : 1 : 1 volume ratio) as the electrolyte. The galvanostatic Li^+ charge and discharge measurements were obtained at room temperature by using Neware Battery Testing System BTS3000 in potential range of 0.01–3.0 *vs.* Li^+/Li at various current densities from ~0.1 to 1 C. Cyclic voltammetry (CV) was performed on EG&G Princeton Applied

Research with a scan rate of 0.5 mV s^{-1}. Electrochemical impedance spectra (EIS) was carried out using Princeton Applied Research Parstat 2273 in the frequency range of 1 MHz to 100 kHz.

Results and discussion

Synthesis of rGO–Mn_3O_4 nanoparticle hybrid materials

The growth of Mn_3O_4 nanoparticles on rGO nanosheets was carried out in two different solvents (Fig. 1). For the preparation of the hybrid materials, Mn_3O_4 nanoparticles were formed *in situ* on rGO by using $MnCl_2 \cdot 4H_2O$ and $KMnO_4$ since Mn^{3+} and Mn^{2+} ions were easily oxidized by electrostatic forces to the free binding sites of negatively charged oxygen-containing functional groups on the GO.[8] In other words, Mn atoms binding with O atoms can be an intermolecular hydrogen bond or a covalent coordination bond, acting as anchor sites for the growth of crystals.[8] These oxygen-containing functional groups also account for uniform dispersion of nanoparticles. The chemical reduction in high pH was carried out using hydrazine hydrate to reduce GOs. The presence of the Mn_3O_4 nanoparticles on the rGO surface prevents the graphene sheet aggregation after reduction process.

Fig. 2 illustrates Mn_3O_4 distribution for three hybrid materials with different Mn_3O_4 contents. TGA curves as shown in Fig. S1† have been used to obtain the mass percent of Mn_3O_4 in the hybrid materials. Mn_3O_4 content is determined

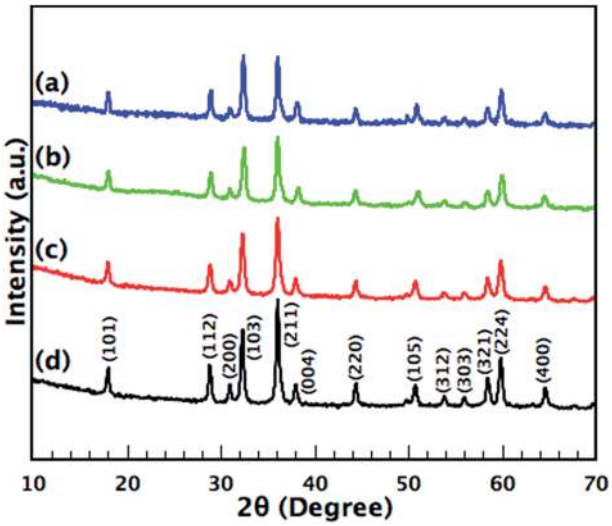

Fig. 3 XRD patterns of the samples (a) MRG1, (b) MRG2, (c) MRG3 and (d) bare Mn_3O_4.

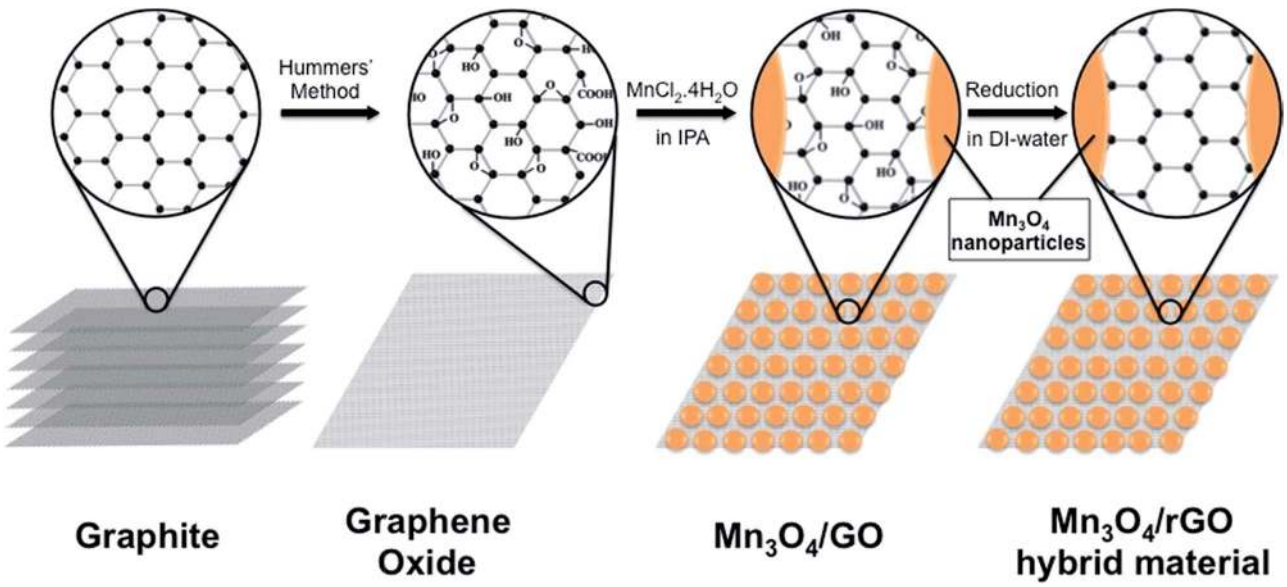

Fig. 1 Preparation route of Mn_3O_4/rGO hybrid materials.

Fig. 2 Schematically illustration of the distribution of nanoparticles on rGO nanosheets with different contents of Mn_3O_4.

to be 36%, 54% and 72% in **MRG1**, **MRG2** and **MRG3**, respectively. Based on the average particle size and nanosheet surface area (BET measurement of rGO), the inter-particle distance is calculated to be 67 nm, 55 nm and 47 nm for **MRG1**, **MRG2** and **MRG3**, respectively (Table S1 in ESI,† detailed explanation on calculations also follows in ESI†). As the content of Mn_3O_4 increases in hybrid material, shorter inter-particle distance (≤1.5 times diameter of nanoparticles)[17] is observed after a threshold which leads to nanoparticle aggregation. On the other hand, large inter-

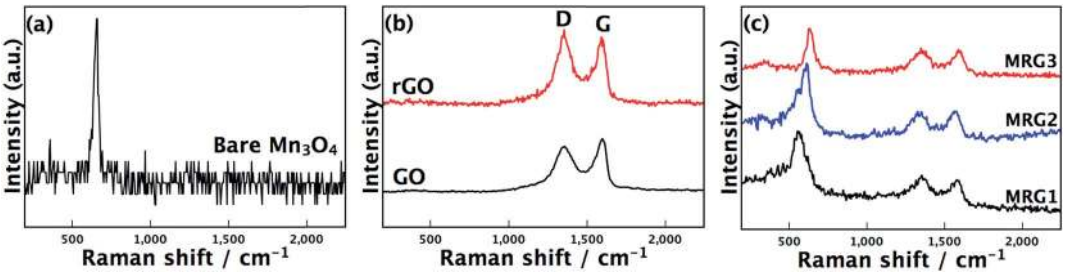

Fig. 4 Raman spectra of (a) bare Mn_3O_4, (b) GO and rGO, and (c) various Mn_3O_4/rGO hybrid materials.

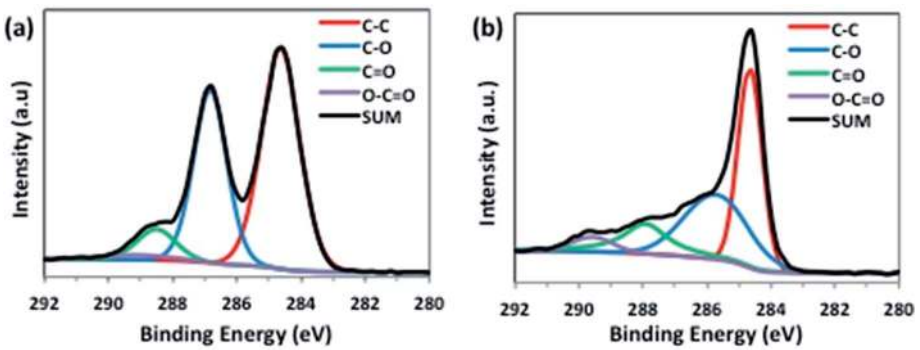

Fig. 5 XPS spectra for the C 1s regions of (a) GO and (b) **MRG2** hybrid material.

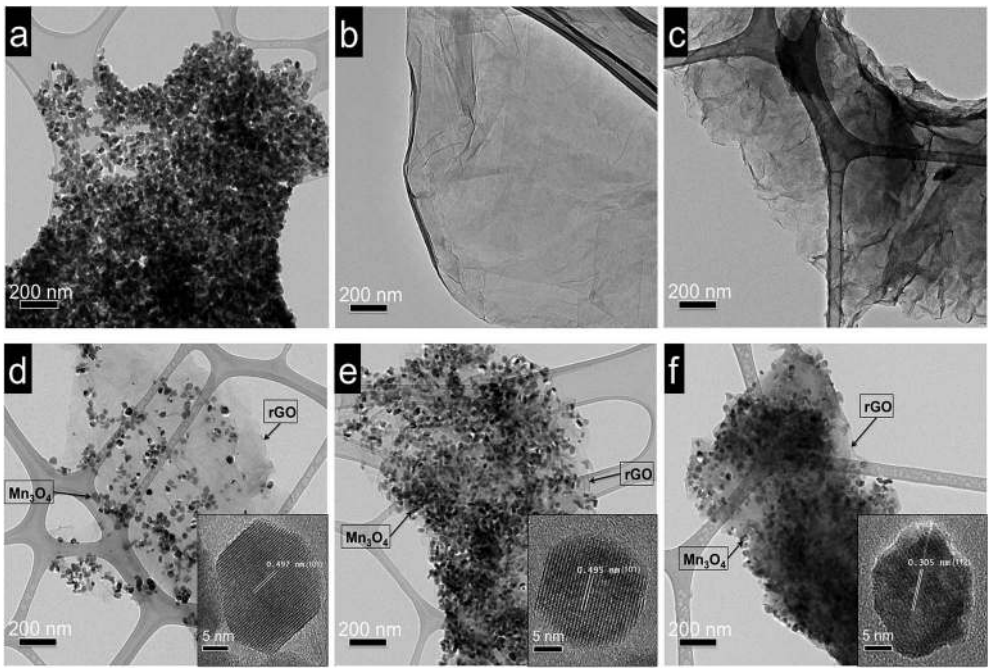

Fig. 6 TEM images of (a) bare Mn_3O_4, (b) GO, (c) rGO, (d) **MRG1**, (e) **MRG2** and (f) **MRG3**.

particle distances can cause nanosheet agglomeration at uncovered locations. Hence, the inter-particle distance has to be optimized for their uniform distribution with minimal nanosheet agglomeration.

Materials characterization of various Mn_3O_4/rGO hybrids

Fig. 3 presents the XRD patterns of bare Mn_3O_4 and Mn_3O_4/rGO hybrid materials with different weight ratios. All diffraction peaks associated with bare Mn_3O_4 and Mn_3O_4/rGO hybrid materials are perfectly indexed to Hausmannite phase of Mn_3O_4 with space group $I4_1/amd$ (JCPDS card: 24-0734). The absence of impurities or other manganese oxide phases indicates the excellent purity of Mn_3O_4 crystalline phase. The average sizes of nanoparticles calculated using the Debye–Scherrer equation[14] were ~30 nm for both bare Mn_3O_4 and Mn_3O_4/rGO hybrid materials. The diffraction peak at around 9° assigned to GO was completely removed from the hybrid materials as shown in Fig. S2.†

Fig. 4 presents the Raman spectra of bare Mn_3O_4, GO, rGO and Mn_3O_4/rGO hybrid materials. As shown in Fig. 4a, the dominant and sharp peak at 638 cm^{-1} demonstrates the Hausmannite phase of crystalline Mn_3O_4 in all hybrid materials. Meanwhile, slight peak shifting of Mn_3O_4 in hybrid materials has been seen, which is most likely due to the oxygen deficiency created during the reduction of GO. In Raman spectroscopy of graphite, sp^2 bonded carbon atoms (E_{2g} phonons) are referred to as the G band, and the defects/disorders are assigned to the D band.[20–22] The ratio of D band (I_D) to G band (I_G) denotes the extent of the defects/disorders in the graphene nanosheets and their crystallite size.[15] GO, rGO and all three different compositions have G band at ~1594 cm^{-1} and D band at ~1351 cm^{-1}. All three hybrid materials show a I_D/I_G ratio vale of ~1.02, which is similar to that of rGO and higher than that of GO, *i.e.* ~0.94, suggesting that the reduction process creates more defects and disorders on rGO. These induced defects/disorders indicate higher activity for nanoparticle deposition. Data thus obtained from Raman are in accordance with XRD results, further indicative of the presence of hybrid materials.

The degree of GO reduction was shown in the XPS measurements by curve fitting as exhibited in Fig. 5. The deconvoluted C1s spectra of GO and Mn_3O_4/rGO hybrid materials are composed of 4 peaks: C–C (284.6 eV), C–O (286.7 eV), C═O (288.6 eV) and O–C═O (288.9 eV).[23] In bare GO, both C–C and C–O peaks are prominent as shown in Fig. 5a. In the case of hybrid materials, a significant decrease occurs in C–O peak, further signifying the removal of oxygen containing groups while C–C peak sustains its dominance (Fig. 5b). This demonstrates that GO has been successfully reduced to rGO before forming a hybrid with Mn_3O_4.

As presented in the SEM images of bare Mn_3O_4, **MRG1**, **MRG2** and **MRG3** (Fig. S3, ESI†), well-crystallized nanoparticles are formed on rGO nanosheets. TEM images are displayed in Fig. 6 for bare Mn_3O_4, GO, rGO, and all three hybrid materials. Fig. 6a shows bare Mn_3O_4 nanoparticles with an irregular shape and a various diameter (~30–50 nm) due to nanoparticle agglomeration. Fig. 6b and c reveal that the GO and rGO are indeed large and transparent nanosheets. The average diameter of the nanoparticles in the hybrid materials is ~30 nm (Fig. 6d–f). Clearly, the nanoparticles on rGO have smaller diameters as each individual particle binds

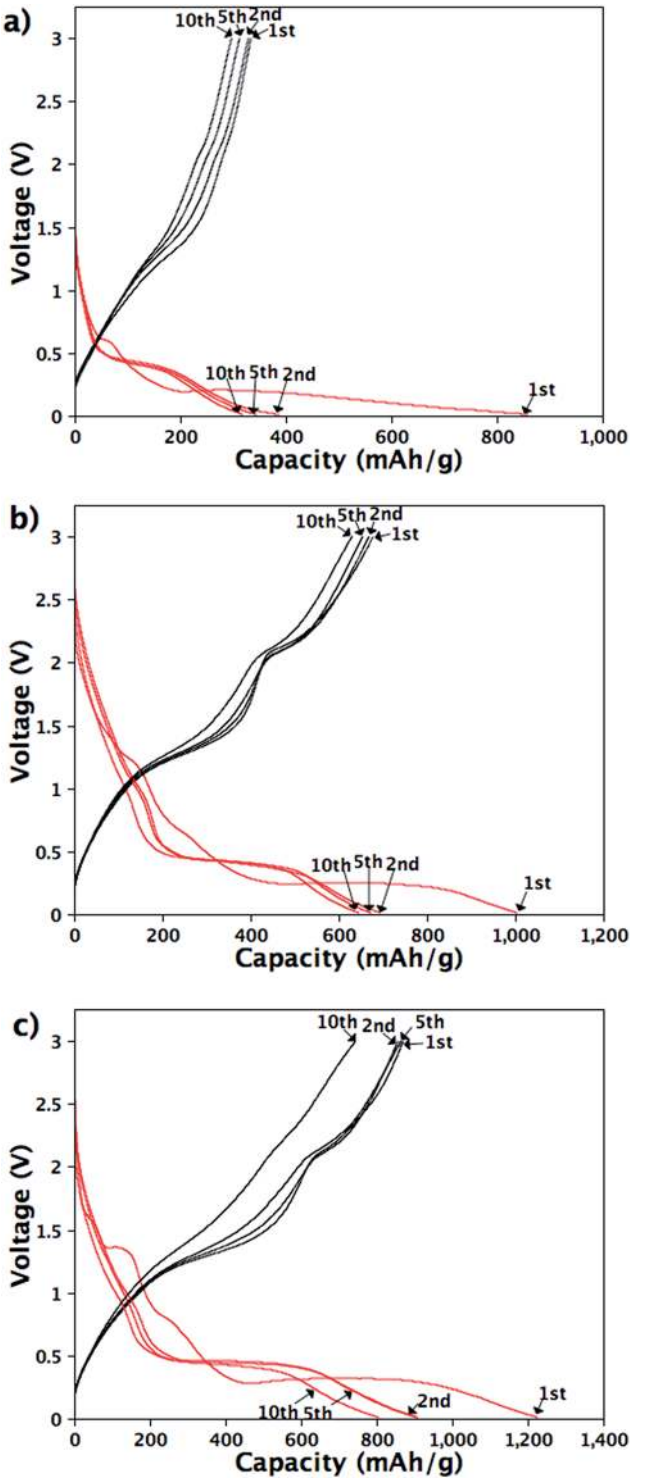

Fig. 7 Galvanostatic discharge (red) and charge (black) of (a) **MRG1**, (b) **MRG2** and (c) **MRG3** electrodes at various cycles and a current density of 120 mA g^{-1}. The potential window is from 3.0 to 0.01 V.

to an active site on rGO rather than pure nanoparticles where each particle attaches to the particle next to it leading to agglomeration and hence, larger diameters. The size distribution histogram for **MRG2** sample (Fig. S4, ESI†) also reveals a mean particle size of 27.8 ± 3.8 nm. In addition, the dispersion of Mn_3O_4 nanoparticles on rGO nanosheets was evident in Fig. 6d–f. Low amounts of Mn_3O_4 lead to insufficient coverage on rGO as seen in Fig. 6d. Conversely, high amounts of Mn_3O_4 lead to their aggregation on rGO nanosheets as shown in Fig. 6f. It can be clearly seen in Fig. 6e that the Mn_3O_4 nanoparticles in **MRG2** are uniformly distributed and densely anchored on the rGO surface compared to both **MRG1** and **MRG3** samples. The HAADF-STEM analysis of **MRG2** sample (Fig. S5, ESI†) also confirms that Mn_3O_4 nanoparticles on the surface of rGO nanosheets are dispersed much better than the **MRG1** and **MRG3** samples. As a result, the electron transfer rate in **MRG2** is high owing to the better conduction channels between nanoparticles and rGO nanosheets.[24]

Electrochemical analysis of various Mn_3O_4/rGO hybrids

Fig. 7 shows the charge/discharge profiles of **MRG1**, **MRG2** and **MRG3** for the first, second, fifth and tenth cycle at a current density of 120 mA g^{-1}. All three electrodes show that lithium insertion occurs below ~0.5 V which corresponds to the redox reaction ($Mn_3O_4 + 8Li^+ + 8e^- = 3Mn + 4Li_2O$).[25] For these hybrid electrode materials with 36, 54, 72% Mn_3O_4, the theoretical capacities are 680, 835 and 989 mA h g^{-1}, respectively. In the electrochemical analysis, the capacity is calculated based on the total weight of the hybrid materials. In the first discharge, **MRG1** (860 mA h g^{-1}), **MRG2** (1005 mA h g^{-1}) and **MRG3** (1226 mA h g^{-1}) hybrid electrodes deliver higher specific capacities than their theoretical capacities primarily because of high surface area available and charge accumulation at active sites which is well documented in the literature for nanomaterials.[26] The first discharge capacity of **MRG3** electrode is the highest among hybrid electrodes; however, **MRG2** electrodes have the lowest irreversible capacity of ~328 mA h g^{-1} in the first cycle, compared to 526 mA h g^{-1} for **MRG1** and 356 mA h g^{-1} for **MRG3**. Understandably, the specific capacity increases with increasing Mn_3O_4 content (note that rGO content decreases at the same time). The irreversible capacity is high for **MRG1** since lithiation at active sites of rGO is irreversible due to low surface coverage of Mn_3O_4. Considerable aggregation of Mn_3O_4 nanoparticles on rGO surface in **MRG3** electrode leads to poor conductivity and hence, higher irreversible capacity than **MRG2**.

The cycling performance of bare Mn_3O_4, rGO and three hybrid electrodes are shown in Fig. 8a and b. Bare Mn_3O_4 electrode delivered a reversible discharge capacity of below 100 mA h g^{-1} with a dramatic decline from cycles 1–40 and the capacity of the rGO electrode was measured to be ~85 mA h g^{-1} after 40 cycles (Fig. 8a). Fig. 8b confirms that **MRG1** and **MRG2** electrodes have cycling stability with a reversible capacity of 270 mA h g^{-1} and 553 mA h g^{-1} after 40 cycles, respectively. The capacity difference between **MRG1** and **MRG2** is primarily due to the mass of Mn_3O_4 as active material on the rGO surface. However, **MRG3** shows a huge drop in reversible capacity after 10 cycles and is ~324 mA h g^{-1} after 40 cycles. The optimum nanoparticle content (**MRG2**) on rGO surface undergoes volume expansion and contraction without fracture and has high stability. **MRG3** has high nanoparticle content without proper volume expansion spaces leading to fracture and huge capacity loss after 10 cycles. The results demonstrate that good cycling performance and high reversible capacity can be obtained *via* optimizing Mn_3O_4 content on rGO.

The rate capability of the three electrodes is presented in Fig. 9. **MRG2** electrode shows a specific capacity of ~330 mA h g^{-1} at a high current density of 1C (Fig. 9b). When the current density is decreased to 0.1C (40 cycles), **MRG2** electrode still delivers a capacity of 531 mA h g^{-1} which is quite close to its initial capacity. Moreover, **MRG1** shows good rate capability like **MRG2**, but its specific capacity is much lower due to the low weight-loading of Mn_3O_4 nanoparticles (Fig. 9a). In addition, **MRG3** shows unstable cycling capability with rate as shown in Fig. 9c, which further indicates that the nanoparticle content does affect cycling stability.

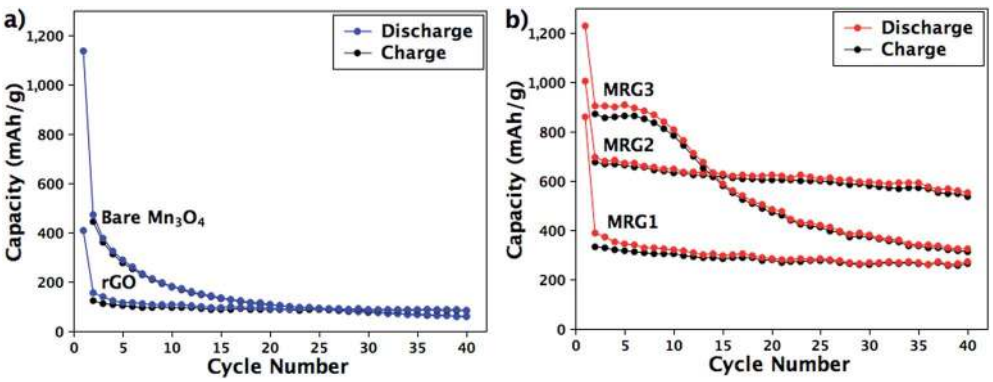

Fig. 8 Cycling performances of (a) bare Mn_3O_4 and rGO electrodes and (b) **MRG1**, **MRG2** and **MRG3** at 120 mA g^{-1}. The potential window is from 3.0 to 0.01 V.

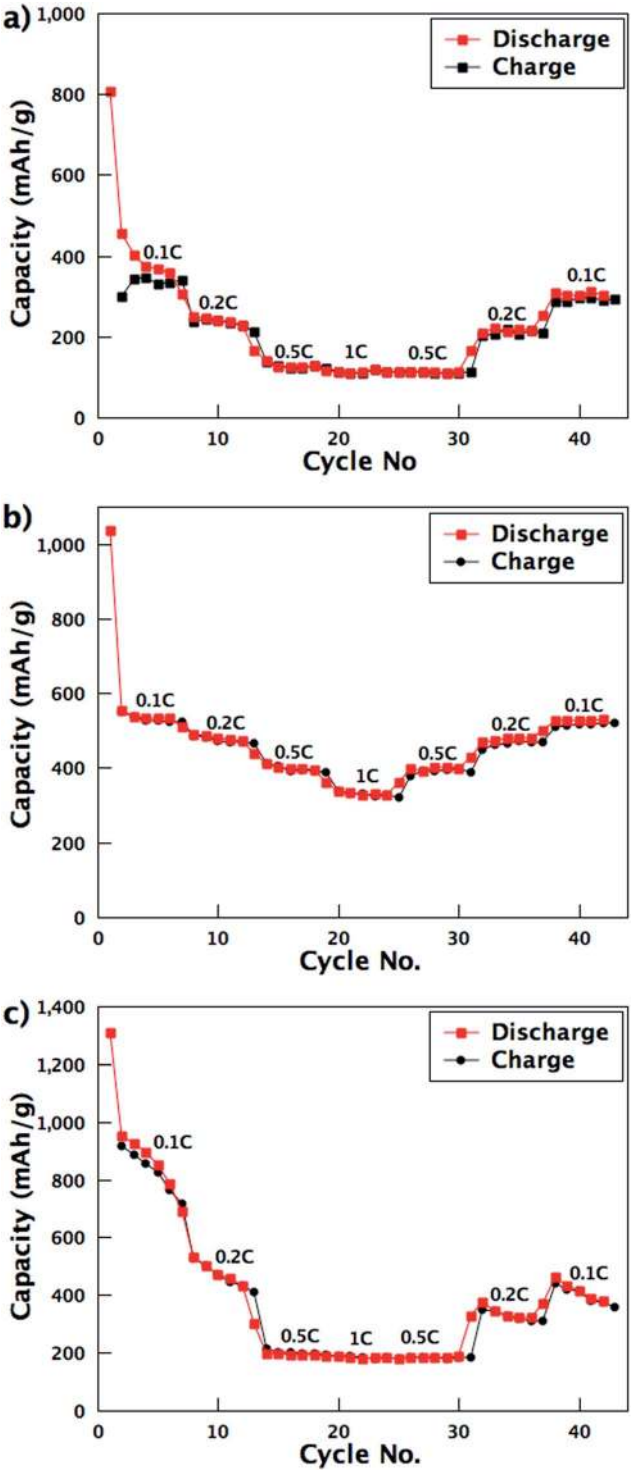

Fig. 9 Capacity retention performance of (a) **MRG1**, (b) **MRG2** and (c) **MRG3** hybrid electrodes at various current density of 0.1C, 0.2C, 0.5C and 1C (1C = 1200 mA g^{-1}) in the potential range of 3.0–0.01 V for 5 cycles per current density.

Fig. 10a–c show the lithiation and delithiation of the electrodes in the voltage range of 0.01–3.0 V. Fig. 10b shows the CV curves for **MRG2** electrode. A small peak around 1.0 V is most likely related to decomposition of electrolyte and formation of SEI film on the electrode surface as well as the reduction of Mn^{3+} to Mn^{2+}. A broad lithiation peak around 0.1 V is ascribed to the main reduction reaction: Mn^{2+} to Mn(0). In the subsequent cycles, this cathodic peak is shifted to a higher voltage of 0.3 V and remains stable, which is prevalent in manganese oxide electrodes and is indicative of the structural changes during lithium insertion in the first cycle.[27] In the delithiation process, Mn(0) is oxidized to Mn^{2+} at around 1.4 V, and a broad delithiation peak appears in the potential range of 2.0–2.5 V attributed to Mn^{2+} to Mn^{3+} oxidation. The overlapped peaks related to oxidation and redox reactions after the second cycle demonstrate good electrochemical reversibility and structural stability for **MRG2** electrode (Fig. 10b). Fig. 10a indicates that **MRG1** electrode shows similar results to that of **MRG2**, but the cathodic/anodic peaks have lower magnitude. This is because of the low active material content of Mn_3O_4 in **MRG1** electrode generating weak current. However, the magnitude of the lithiation/delithiation peaks for **MRG3** electrode decrease dramatically in 10 cycles, which further confirms that the reversible capacity of **MRG3** decays with cycling (Fig. 10c).

Electrochemical impedance measurements have been carried out before discharge, 10^{th} full discharge (120 mA g^{-1}) and the 40^{th} full discharge (120 mA g^{-1}) for all three hybrid electrodes in the frequency range of 10^6 to 0.01 Hz. The overall cell resistance is shown on the intercept between the end of semicircle and the Z' axis. It can be seen in Fig. 10d–f that **MRG2** and **MRG3** hybrid electrodes possess lower cell resistance and the highest electrical conductivity in the discharge than **MRG1** hybrid electrodes. This is ascribed to the nanoparticle network that enhances electrical conductivity. It can be concluded that the weight of active anode materials loading on the rGO is an important parameter in order to achieve good reversible capacity and stable structure during lithium insertion and extraction for LIBs. Thus, the electrochemical performance measurements clearly indicate that **MRG2** is the best candidate as a hybrid anode material for LIBs compared to **MRG1** and **MRG3**.

Conclusions

A comprehensive investigation of the electrochemical performance of Mn_3O_4/rGO hybrid as an anode material for LIBs is discussed. Mn_3O_4/rGO hybrid-composite materials were prepared through a facile *in situ* synthetic route *via* encapsulating nanosized Mn_3O_4 particles on the rGO matrix. In order to demonstrate the structural effect, Mn_3O_4 nanoparticles have been grown with three different loading ratios onto rGO nanosheets. **MRG2** electrode material exhibited the best electrochemical performance compared to other two electrodes, which showed a high reversible capacity of over 550 mA g^{-1} after 40 cycles at a current density of 120 mA g^{-1}. This is due to the optimized loading of Mn_3O_4 and uniform dispersion in rGO in **MRG2**, which eliminated the aggregation of the Mn_3O_4 nanoparticles and stacking of rGO nanosheets. We believe that this work can pave way for further research on metaloxide/graphene composites as anode materials for high performance LIBs.

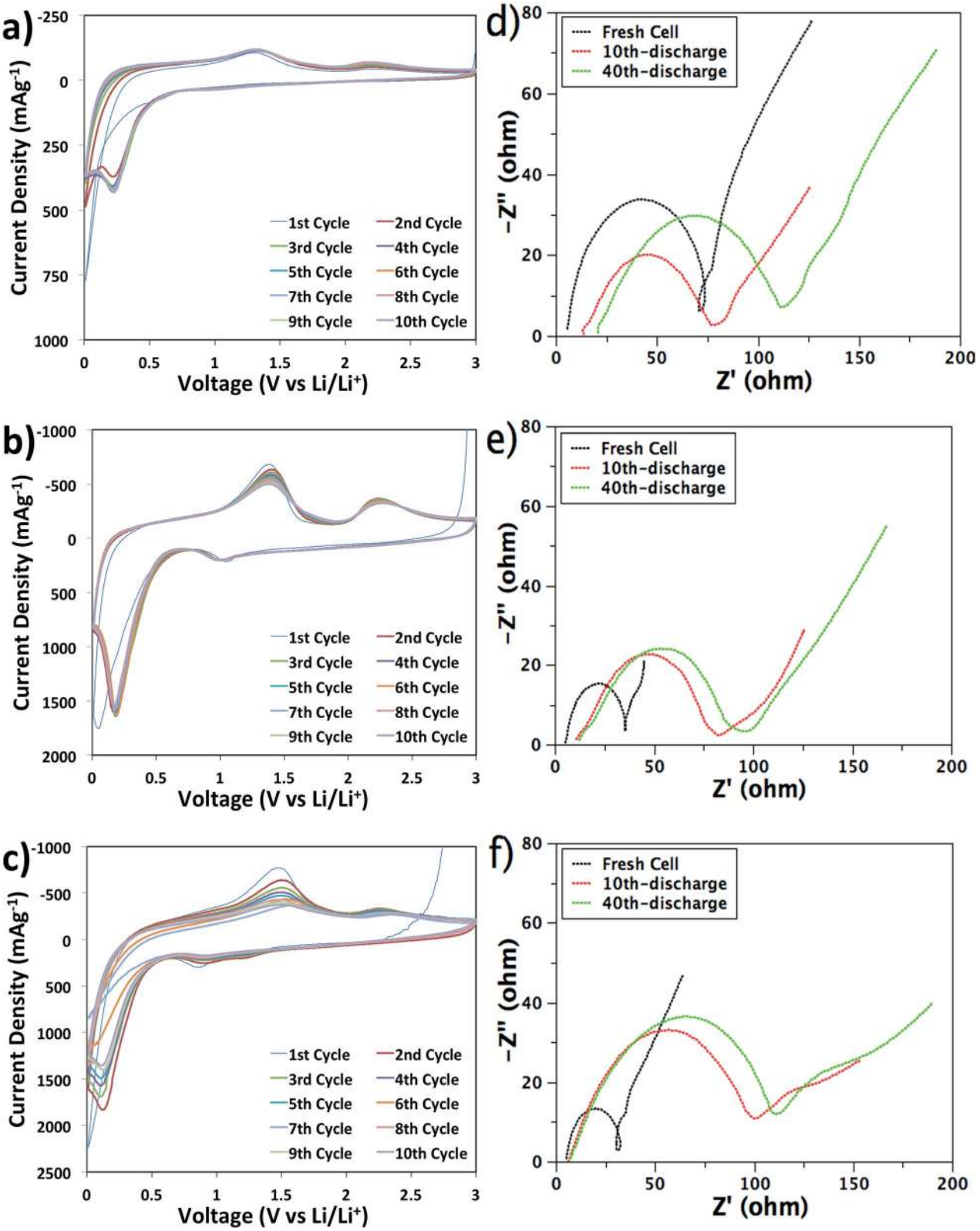

Fig. 10 Cyclic voltammetry (CV) performance of (a) **MRG1**, (b) **MRG2** and (c) **MRG3** hybrid electrodes at scan rate of 0.5 mV s^{-1} for 10 cycles. Nyquist plots of (d) **MRG1**, (e) **MRG2** and (f) **MRG3** at cell states of before discharge, 10^{th} discharge at 120 mA g^{-1} and 40^{th} discharge at 120 mA g^{-1} in the frequency range of 10^6 to 0.01 Hz.

Acknowledgements

I. A. A. acknowledges the support by a fellowship funded by Republic of Turkey Ministry of National Education for graduate programs.

References

1 A. S. Aricò, P. Bruce, B. Scrosati, J.-M. Tarascon and W. van Schalkwijk, *Nat. Mater.*, 2005, **4**, 366–377.
2 J.-M. Tarascon, *Philos. Trans. R. Soc., A*, 2010, **368**, 3227–3241.
3 M. Armand and P. Touzain, *Mater. Sci. Eng.*, 1977, **31**, 319–329.
4 M. Winter, J. O. Besenhard, M. E. Spahr and P. Novák, *Adv. Mater.*, 1998, **10**, 725–763.
5 J. R. Dahn, T. Zheng, Y. Liu and J. S. Xue, *Science*, 1995, **270**, 590–593.
6 A. K. Geim and K. S. Novoselov, *Nat. Mater.*, 2007, **6**, 183–191.
7 S.-M. Paek, E. Yoo and I. Honma, *Nano Lett.*, 2009, **9**, 72–75.
8 S. Chen, J. Zhu, X. Wu, Q. Han and X. Wang, *ACS Nano*, 2010, **4**, 2822–2830.
9 K. Evanoff, A. Magasinski, J. Yang and G. Yushin, *Adv. Energy Mater.*, 2011, **1**, 495–498.
10 P. Poizot, S. Laruelle, S. Grugeon, L. Dupont and J. M. Tarascon, *Nature*, 2000, **407**, 496–499.
11 H. Wang, L.-F. Cui, Y. Yang, H. Sanchez Casalongue, J. T. Robinson, Y. Liang, Y. Cui and H. Dai, *J. Am. Chem. Soc.*, 2010, **132**, 13978–13980.
12 D. Pasero, N. Reeves and A. West, *J. Power Sources*, 2005, **141**, 156–158.
13 M. M. Thackeray, W. I. F. David, P. G. Bruce and J. B. Goodenough, *Mater. Res. Bull.*, 1983, **18**, 461–472.
14 H. Wang, L.-F. Cui, Y. Yang, H. Sanchez Casalongue, J. T. Robinson, Y. Liang, Y. Cui and H. Dai, *J. Am. Chem. Soc.*, 2010, **132**, 13978–13980.
15 L. Wang, Y. Li, Z. Han, L. Chen, B. Qian, X. Jiang, J. Pinto and G. Yang, *J. Mater. Chem. A*, 2013, 8385–8397.
16 I. Nam, N. D. Kim, G.-P. Kim, J. Park and J. Yi, *J. Power Sources*, 2013, **244**, 56–62.
17 B. J. Dimitrijevic, K. E. Aifantis and K. Hackl, *J. Power Sources*, 2012, **206**, 343–348.
18 N. Liu, H. Wu, M. T. McDowell, Y. Yao, C. Wang and Y. Cui, *Nano Lett.*, 2012, **12**, 3315–3321.
19 W. S. Hummers and R. E. Offeman, *J. Am. Chem. Soc.*, 1958, **80**, 1339.
20 C. N. R. Rao, K. Biswas, K. S. Subrahmanyam and A. Govindaraj, *J. Mater. Chem.*, 2009, **19**, 2457.
21 O. M. Maragó, F. Bonaccorso, R. Saija, G. Privitera, P. G. Gucciardi, M. A. Iatì, G. Calogero, P. H. Jones, F. Borghese, P. Denti, V. Nicolosi and A. C. Ferrari, *ACS Nano*, 2010, **4**, 7515–7523.
22 D. M. Basko, S. Piscanec and A. C. Ferrari, *Phys. Rev. B: Condens. Matter Mater. Phys.*, 2009, **80**, 165413.
23 L. Wang, Y. Li, Z. Han, L. Chen and B. Qian, *J. Mater. Chem. A*, 2013, 1–14.
24 L. Zhu, S. Zhang, Y. Cui, H. Song and X. Chen, *Electrochim. Acta*, 2013, **89**, 18–23.
25 Z.-S. Wu, W. Ren, L. Wen, L. Gao, J. Zhao, Z. Chen, G. Zhou, F. Li and H.-M. Cheng, *ACS Nano*, 2010, **4**, 3187–3194.
26 S.-H. Park and W.-J. Lee, *Sci. Rep.*, 2015, **5**, 9754.
27 J. Guo, Q. Liu, C. Wang and M. R. Zachariah, *Adv. Funct. Mater.*, 2012, **22**, 803–811.

